

# **Ionic Liquid based Fluoropolymer Solid Electrolytes for Lithium-ion Batteries**

Serra, J.P., Pinto, R.S., Barbosa, J.C., Correia, D.M., Gonçalves, R., Silva, M.M., Lanceros-Mendez, S., Costa, C.M.;

**Abstract:** Composite materials based on ionic liquids (ILs) / poly(vinylidene fluoride) (PVDF) and their copolymers have emerged as an interesting approach to develop high ionic conductivity solid polymer electrolytes (SPEs) for lithium-ion battery application. This work reports the development of SPEs based on fluoropolymers, PVDF and poly(vinylidene fluoride co-hexafluoropropylene), PVDF-HFP, containing different ILs: 1-ethyl-3-methylimidazolium bis (trifluoromethylsulfonyl) imide ([EMIM][TFSI]) and 1-butyl-3-methylimidazolium thiocyanate ([BMIM][SCN]). The influence of IL type and content on the morphological, wettability, physical-chemical, thermal, mechanical and electrochemical properties were evaluated. It is shown that, independently of the polymer matrix, both ILs improve surface wettability and increase the polar  $\beta$  phase content and crystallinity degree of the polymers. The mechanical properties show that the incorporation of IL in the composites results in a plasticizing behaviour.

Further, the [BMIM][SCN]/PVDF-HFP with 40 wt.% IL content shows the best room temperature ionic conductivity of  $0.15 \text{ mS.cm}^{-1}$  with excellent electrochemical stability in the 0.0 - 5.0 V potential window. The initial discharge capacity value at C/8-rate is  $148 \text{ mAh.g}^{-1}$  and  $124 \text{ mAh.g}^{-1}$  for the [BMIM][SCN]/PVDF and [BMIM][SCN]/PVDF-HFP composites, respectively, with high coulombic efficiency (98%). At C/8-rate, batteries with [BMIM][SCN]/PVDF-HFP show the lowest capacity fade (16 % after 50 cycles) of the prepared composites.

Thus, it is demonstrated the suitability of developing SPEs based on IL and fluorinated polymers for the next generation of solid-state room temperature lithium-ion batteries.

**Keywords:** Batteries, ionic liquids, PVDF, PVDF-HFP, solid polymer electrolytes.

## 1. Introduction

Solid electrolytes are among the key issues in future battery technologies [1, 2]. A battery converts chemical energy into electrical energy through electrochemical redox reactions [3]. The first battery was developed by Alessandro Volta in 1800, using zinc and silver electrodes and brine-soaked cloth as separator [4]. Lithium technology only started to be developed in the 70's of the XX century using titanium sulphide and metallic lithium as electrodes, the first commercial lithium-ion batteries (LIBs) being developed in 1991 by Sony [5]. The main advantages of these type of batteries, when compared to other commercial batteries, rely on the higher energy density per mass and volume. Further, they are lighter, cheaper, and show a higher number of charge/discharge cycles [6].

LIBs are composed of three main components: two electrodes (cathode and anode) and a separator, which is generally soaked in a liquid electrolyte, which is responsible for providing ionic conductivity to the separator [7]. The separator avoids the occurrence of short-circuits between the electrodes and serves as a means of ions exchange between them. Moreover, the separator allows to control the mobility and the number of ions. For this reasons, the separator has an essential role in batteries [8]. Additionally, a set of requirements is essential to determine the performance of the separators, including chemical, thermal and mechanical stability, porosity, electrical resistance, wettability and resistance to electrochemical degradation [8]. Despite the advantages of LIB, the use of liquid electrolytes increases the risk of future complications, since this component is flammable, increasing the risk of explosions or combustions. Further, it is toxic and dangerous for the environment [9]. To overcome the aforementioned disadvantages, solid electrolytes have been intensively studied in the form of solid polymeric electrolytes and solid ceramic electrolytes [10].

Solid polymer electrolytes (SPE's) can be defined as solvent-free salt solutions in a polymer host material with high mechanical stability. Typically, SPE's consist of a polymeric matrix combined with an ionic conductive filler (carbonaceous, lithium salts or ionic liquids) aiming to increase the necessary ionic conductivity of SPE's [11]. Several advantages are associated to SPE's over the liquid electrolytes, such as increased safety, long lifetime, low charge time and low internal corrosion. However, these SPE's also present some limitations like the lack of high enough ionic conductivity to work properly, being limited to high temperatures, the interface between the electrodes and the difficulty to maintain the structural integrity of the SPE when subjected to stresses in the

electrochemical cycling (cracks in the structure). SPE's for LIB applications need a high ionic conductivity above  $10^{-4}$  S.cm<sup>-1</sup> at room temperature [12, 13].

The most common polymers used as SPE's in lithium-ion batteries are poly(propylene) (PP), poly(ethylene) (PE), poly(ethylene oxide) (PEO), poly(acrylonitrile) (PAN) and poly(vinylidene fluoride) (PVDF) and its copolymer poly(vinylidene fluoride-co-hexafluoropropylene) (PVDF-HFP) [8].

Different polymer composites with different fillers BaTiO<sub>3</sub> [14], Al<sub>2</sub>O<sub>3</sub> [15], SiO<sub>2</sub> [16], TiO<sub>2</sub> [17]), carbonaceous (graphene oxide [18], carbon nanotubes [19]), lithium salts (LiBF<sub>4</sub> [20], LiPF<sub>6</sub> [21], LiClO<sub>4</sub> [22], LiTFSI [23], [EMIM][TFSI] [24] or [BMIM][TFSI] [25]) have been developed as SPEs for batteries [26]. Most SPE's reported in the literature show low ionic conductivity value at room temperature caused by poor diffusion of ions in a solid matrix, as is observed for polyimide matrix PI with 100 % [BMIM][TFSI] and 60 % LiTFSI membranes in which the ionic conductivity can be up to  $1.73 \times 10^{-5}$  S.cm<sup>-1</sup> at room temperature and reaches 1.26 mS.cm<sup>-1</sup> at 80 °C. Typically, the cycling behavior of SPE is tested at temperatures above 60°C that limit their applicability in solid state batteries, therefore the goal of this work is the production of new SPEs based on different ILs with a high ionic conductivity value above 5 mS.cm<sup>-1</sup> at room temperature.

In this context, the use of fluoropolymers from PVDF (CH<sub>2</sub>-CF<sub>2</sub> monomer) and copolymers as polymer matrix seem advantageous based on their semi crystalline and highly polar nature [13]. PVDF is a semi-crystalline polymer, presents high dielectric constant and large electroactive response, including ferroelectric, piezoelectric and pyroelectric effects. This semi-crystalline polymer presents different crystalline phases ( $\alpha$ ,  $\beta$ ,  $\gamma$  and  $\delta$ ) [14], the being  $\beta$ -phase the one with the highest dipolar moment and electroactive properties [13, 15, 16]. In fact, composites based on PVDF containing ionic liquids (ILs) have emerged as an interesting approach to the development of SPE's. ILs are commonly defined as organic salts composed by cations and anions with a low melting temperature, high thermal, chemical and ionic conductivity and electrochemical stability [27-29]. Another interesting property of ILs relies on its non-flammability and non-volatility, particularly relevant in battery applications [30].

IL/PVDF composites were prepared by the solution-cast method, in which the incorporation of ILs into the polymer matrix increases dc conductivity [31].

Typically, IL/PVDF composites show a low ionic conductivity value below  $10^{-4}$  S/cm and other fillers are added to increase ionic conductivity. In this context, the focus of this

study is the development of composites based on fluoropolymers, PVDF and PVDF-HFP, containing different ILs, in order to obtain high ionic conductivity. Further, the composites were produced by solution casting, a low cost and scalable production method. To achieve this, the ILs 1-ethyl-3-methylimidazolium bis (trifluoromethylsulfonyl) imide ([EMIM][TFSI]) and 1-butyl-3-methylimidazolium thiocyanate ([BMIM][SCN]) were studied. The influence of the IL type, content, and fluorinated matrix on the morphological, physical-chemical, thermal, mechanical, and electrochemical properties of the composites were studied. Ionic conductivity value, electrochemical window stability and charge-discharge performance of SPE in cathodic C-LiFePO<sub>4</sub> half-cells were evaluated to demonstrate the potential of the developed composites as SPEs for a new generation of solid-state lithium-ion batteries.

## 2. Experimental section

### 2.1. Materials

Poly(vinylidene fluoride) (PVDF) (Kynar PVDF HSV900) and the PVDF co-polymer poly(vinylidene fluoride-co-hexafluoropropylene (PVDF-HFP) (Kynarflex PVDF-HFP 2801-00107) were purchased from Arkema. N,N-dimethylformamide (99%), DMF, and N-Methyl-2-pyrrolidone (99%), NMP were obtained from Merck, and the ionic liquids 1-ethyl-3-methylimidazolium bis (trifluoromethylsulfonyl) imide, 99% ([EMIM][TFSI]) and 1-butyl-3-methylimidazolium thiocyanate), >98% ([BMIM][SCN]) were supplied by Iolitec.

Table 1 illustrates the chemical structure and main relevant properties of the different ILs used in this work.

### 2.2. Film preparation

Polymer films were prepared by a solvent casting process. Neat PVDF and PVDF-HFP films were obtained after the polymer dissolution in DMF (15/85 wt.%) under magnetic stirring at 40 °C. After complete polymer dissolution, the solution was spread on a glass substrate followed by solvent evaporation in an oven (PSelecta) at 210 °C during 10 min. This preparation procedure allows to obtain homogenous non-porous polymer films [32]. IL/PVDF and IL/PVDF-HFP composites were prepared by a similar procedure. Previous to the PVDF and PVDF-HFP dissolution, different IL concentrations (10 ,20 and 40 wt.%) of [EMIM][TFSI] and 40 wt.% of [BMIM][SCN] were dispersed in DMF. Then, PVDF or PVDF-HFP were added, independently, to the IL/DMF solution. After complete polymer dissolution, the solution was spread on a glass and placed in the oven (PSelecta) at 210 °C, for 10 min, leading to films with a final thickness of  $\sim 60\mu\text{m} \pm 20 \mu\text{m}$ . Figure 1 shows the schematic representation of the procedure used to prepare the IL/PVDF and IL/PVDF-HFP composite films.

### 2.3. Sample characterization

The morphology of the samples was evaluated by scanning electron microscopy (SEM), with a FEI Nova 200 (FEG/SEM); EDAX - Pegasus X4M (EDS/EBSD)) with an accelerating voltage of 10 kV. Previously to analysis, the samples were coated with a gold layer (Polaron, model SC502).

The water contact angle of the samples was measured using a Dataphysics Contact Angle System OCA20 using ultrapure water drop (3 $\mu$ L) for the test. The measurements were carried out at three different spots on the film and the contact angle was determined using the measuring software.

Fourier transform infrared (FTIR) spectroscopy in attenuated total reflection (ATR) mode was performed with a Jasco FT/IR-6100 from 4000 to 600  $\text{cm}^{-1}$  using 64 scans with a resolution of 4  $\text{cm}^{-1}$ .

The amount of the electroactive  $\beta$  phase was calculated from the FTIR/ATR data using equation 1:

$$F(\beta) = \frac{A_{\beta}}{\left(\frac{K_{\beta}}{K_{\alpha}}\right)A_{\alpha} + A_{\beta}} \quad (1)$$

where  $A_{\alpha}$  and  $A_{\beta}$  represent the absorptions at 766 and 840  $\text{cm}^{-1}$  and  $K_{\alpha}$  ( $6.1 \times 10^4 \text{ cm}^2 \text{ mol}^{-1}$ ) and  $K_{\beta}$  ( $6.1 \times 10^4$  and  $7.7 \times 10^4 \text{ cm}^2 \text{ mol}^{-1}$ ) are the corresponding absorption coefficient [33].

Differential scanning calorimetry (DSC) measurements were carried out in a Perkin-Elmer DSC 6000 equipment in the temperature range between 25  $^{\circ}\text{C}$  and 200  $^{\circ}\text{C}$  at 10  $^{\circ}\text{C} \cdot \text{min}^{-1}$  under nitrogen atmosphere. The degree of crystallinity ( $\Delta X_c$ ) was evaluated from the DSC thermograms using equation 2:

$$\Delta X_c = \frac{\Delta H}{x\Delta H_{\alpha} + y\Delta H_{\beta}} \quad (2)$$

in which  $\Delta H$  corresponds to the melting enthalpy of the sample, and  $\Delta H_{\alpha}$  and  $\Delta H_{\beta}$  the melting enthalpies of  $\alpha$  phase (93.07  $\text{J g}^{-1}$ ) and  $\beta$  phase (103.4  $\text{J g}^{-1}$ ) PVDF, respectively.  $x$  and  $y$  are the  $\alpha$  and  $\beta$  phase content respectively [33].

Mechanical stress-strain measurements were carried out in a Shimadzu Autograph AG-IS universal testing set-up with a load cell of 50 N. Three measurements were performed for each sample at a stretching speed of 1 mm per minute.

Electrochemical impedance spectroscopy (EIS) measurements were performed with an Autolab PGSTAT-12/30 electrometer amplifier, at 50 frequencies between 0.5 Hz and 65 kHz in the temperature range from 25 °C to 100 °C at approximately 7 °C intervals. The samples were placed between two gold electrodes inside a Buchi TO-51 oven. The ionic conductivity ( $\sigma_i$ ) of the composite films was calculated after [19]:

$$\sigma_i = d/R_b \times A \quad (3)$$

where  $R_b$  is the bulk resistance,  $d$  is the thickness and  $A$  is the area of the film.

The electrochemical stability of the films was evaluated through cyclic voltammetry (CV) in the two-electrode cell configuration with a gold microelectrode as working electrode and a lithium disk (Aldrich, 99.9 %; 19 mm diameter, 0.75 mm thick) as counter electrode. CV was carried out within a dry argon-filled glove-box and inside a Faraday cage using an Autolab PGSTAT-12 (Eco Chemie) equipment between 0.0 and 5.0 V at a scan rate of 0.1 mV.s<sup>-1</sup>.

#### *2.4. Cathode preparation and battery fabrication and evaluation*

The cathode was prepared using 80 wt.% C-LiFePO<sub>4</sub>, 10 wt.% carbon black and 10 wt.% PVDF. The electrode slurry was then casted on aluminum foil by doctor-blade technique and dried at 100 °C for 2 h as explained in detail in [34]. The active mass loading was ~ 1-1.5 mg.cm<sup>-2</sup>.

Swagelok type Li/C-LiFePO<sub>4</sub> half-cells were assembled in a home-made argon-filled glove box and prepared using the IL/composites films as SPE's (10 mm diameter), metallic lithium (8 mm diameter) as an anode and C-LiFePO<sub>4</sub> based electrode as a cathode (8 mm diameter) as is illustrated in Figure 2. Charge-discharge tests were obtained at room temperature in the voltage range from 2.5 to 4.2 V at C/8 (C = 170 mAh.g<sup>-1</sup>) during 50 cycles using a Landt CT2001A Instrument.

The electrical properties of Li/C-LiFePO<sub>4</sub> half-cells were measured by electrochemical impedance spectroscopy (EIS) with an Autolab PGSTAT12 instrument, in the frequency range from 10 mHz to 1 MHz, with a signal amplitude of 10 mV.

### 3. Results and discussion

#### 3.1. Morphological characterization

The morphology of the developed neat polymers and the corresponding IL composites was evaluated by SEM. Figure 3 shows representative images for the pristine polymer and the corresponding IL composites with the maximum IL content of 40 wt.%.

Figure 3 shows that, independently of PVDF type and IL content (see supplementary information S1), neat PVDF (Figure 3a) and PVDF-HFP (Figure 3d) films show a compact and non-porous homogeneous surface. Upon the incorporation of 40 wt.% of the different ILs, no relevant changes occur in any of the samples, in the sense that an overall compact non-porous microstructure is observed in all samples. Nevertheless, the incorporation of both [EMIM][TFSI] and [BMIM][SCN] in PVDF (Figures 3b and c) leads to an increasing number of spherulites. This fact is an indication that both ILs acts as nucleating agents leading to a higher number of crystallization nuclei and, therefore, to a larger number of smaller spherulites and spherulite interfaces with well-defined borders [35, 36]. On the other hand, the incorporation of both IL in the PVDF-HFP matrix shows a related effect of more marked morphological features (Figure 3e and f) than the pristine polymer, but in a lower extent, due to the lower degree of crystallinity of the polymer, as we will discuss later in section 3.3.

#### 3.2. Surface wettability

The influence of IL type and content on the surface wettability of the samples was evaluated by contact angle measurements. Figure 4a shows that pristine PVDF shows a contact angle of  $85.0 \pm 2.8^\circ$ , a value that decreases with the incorporation of [EMIM][TFSI] to a minimum of  $66.7 \pm 4.3^\circ$  for the sample with 20 wt.% IL content. This increase in the surface wettability of the samples results from IL-polymer interactions, which promote a decrease in the surface tension of the films [37, 38]. Further, the hygroscopic nature of IL plays an important role in the decrease of the surface wettability [38]. The small increase of the surface wettability for the [EMIM][TFSI]/PVDF film containing 40 wt.% IL content is related to some saturation of the IL effectively incorporation in the polymer and its migration to the surface of the polymer [37].

It is to notice that the aforementioned effect is independent of the IL type, being also observed for the [BMIM][SCN] incorporated in the PVDF (Figure 4b). In fact, the



decrease of the water contact angle is even more evident for composites containing [BMIM][SCN]. Further, the results are also similar, independently of the polymer matrix, neat PVDF-HFP showing a water contact angle of 91° that decreases to a minimum of 67° with the incorporation of 40 wt.% [EMIM][TFSI].

### 3.3. Polymer phase content, thermal and mechanical properties

The influence of the incorporation of the ILs on the phase content of the polymers was evaluated from the FTIR/ATR spectra presented in Figure 5.

Figure 5a shows that, independently of the IL content, the main absorption bands characteristic of PVDF are presented in the FTIR spectra. The absorption bands at 976, 795, 763 and 678  $\text{cm}^{-1}$  are attributed to the stretching vibrations of the  $\text{CF}_2$  and  $\text{CH}_2$  groups of the polymer and are characteristic of the  $\alpha$  phase of the PVDF [33, 39]. With increasing [EMIM][TFSI] content up to 40 wt.%, the intensity of the absorption band at 840  $\text{cm}^{-1}$ , characteristic of the  $\text{CH}_2$  groups and attributed to the electroactive  $\beta$  phase, increases [40]. A small amount of  $\gamma$  - PVDF is observed in the [EMIM][TFSI]/PVDF composites, as indicated by the absorption bands at 1232 and 813  $\text{cm}^{-1}$  [39]. The [EMIM][TFSI] characteristic absorption bands appear at 1479  $\text{cm}^{-1}$ , attributed to the C-H bending of the methyl group, at 1051  $\text{cm}^{-1}$ , corresponding to the asymmetrical S-N-S stretching mode, and at 1349, 1132 and 612  $\text{cm}^{-1}$ , ascribed to the asymmetric and symmetric stretching vibration mode of the  $\text{SO}_2$  group. The vibration band at 740  $\text{cm}^{-1}$  is attributed to the CIS anion conformation. Similarly to PVDF, also the main absorption bands of PVDF-HFP [41] are found in the corresponding composites. With respect to the main absorption band of [BMIM][SCN] in the PVDF-HFP composites, it is presented at 2056  $\text{cm}^{-1}$  and is ascribed to the  $[\text{SCN}]^-$  anion.

It is to notice that, for both IL types, the cations are from the imidazolium family, presenting to the composites also the stretching vibrations characteristics of the NC(H)N and CCH groups at  $\sim 843 \text{ cm}^{-1}$  of the imidazolium ring [42]. It is to notice that the relative low intensity of this IL absorption band [42], leads that the absorption band at 840  $\text{cm}^{-1}$  is mostly attributed to the contribution of the PVDF  $\beta$  phase. In fact, it is to notice that both composites present another absorption band characteristic of the electroactive  $\beta$  phase at 1275  $\text{cm}^{-1}$  [43]. The intensity of this absorption band increases with increasing IL content (see Figure 5a for the [EMIM][TFSI]/PVDF composites), showing that

effectively both PVDF and PVDF-HFP composites crystallize in the electroactive  $\beta$  phase upon ILs incorporation in the polymer matrix.

The quantification of the electroactive  $\beta$  phase was achieved using Equation 1, as indicated in [33]. The obtained values are presented in Table 2 and demonstrate an increase in the  $\beta$ -phase content with the incorporation of both ILs, being independent of the IL type and fluorinated matrix. The nucleation of the electroactive phase of PVDF by incorporation of IL's has been in fact, already discussed [44], being attributed to the electrostatic ion-dipole interactions between the charges of ILs and the dipoles of the PVDF chain. As observed for PVDF, there is a strong increase of the electroactive phase content, up to 83%, with the incorporation of 10 wt.% of the IL, being independent on further increasing IL content. This effect is independent of the fluorinated matrix, being obtained similar results for PVDF-HFP. The highest  $\beta$ -phase content is observed for the [BMIM][SCN]/polymer composites, which fully crystallize in the electroactive phase. The influence of the incorporation of the ILs in the fluorinated matrix also leads to variations in thermal properties and the degree of crystallinity, as evaluated from the DSC scans presented in Figure 6.

Figure 6 shows that DSC scans of neat polymers are characterized by a single melting peak, which occurs at 168 °C for PVDF and 144 °C for neat PVDF-HFP.

DSC scans for IL/polymer composites show similar behaviour for the pristine polymer, but decreasing the melting temperature with the IL incorporation and content, as presented in Figure 6a for the incorporation of [EMIM][TFSI] and Figure 6b for the incorporation of [BMIM][SCN]. Table 2 shows that the melting temperature decreases from 162 to 152 °C for the PVDF with the incorporation of 40 wt.% of [EMIM][TFSI] or [BMIM][SCN]. Further, the same behaviour is observed for PVDF-HFP composites. The observed decrease in the melting temperature for the IL/PVDF and IL/PVDF-HFP composite samples indicates a crystalline phase destabilization, hindering the crystallization process as a consequence of the electrostatic interactions between the [EMIM][TFSI] and [BMIM][SCN] and the polymer matrix [37, 44]. Additionally, the influence of both ILs on the degree of crystallinity was evaluated through Equation 2, as presented in Table 2.

Independently of the fluorinated matrix and IL content, the degree of crystallinity generally slightly decreases with the incorporation of IL when compared to the neat polymer. For PVDF, the degree of crystallinity slightly decreases from 35 % to 28 % with

the incorporation of 40 wt.% [EMIM][TFSI], whereas the decrease is even lower with the incorporation of 40 wt.% [BMIM][SCN]. The decrease in the degree of crystallinity are larger for the incorporation of [EMIM][TFSI] and [BMIM][SCN] in PVDF-HFP, reaching degrees of crystallinity as low as 12 and 16 %, respectively for the samples with 40 wt.% content. Thus, these results indicate that both ILs act as nucleating agents during the crystallization process as a result of IL-polymer interactions, leading to the increase of the lamellar size of spherulites [44].

The variation in the degree of crystallinity is typically reflected in the mechanical properties of the materials. The mechanical properties of the IL / fluorinated polymer composites were evaluated by tensile tests. The obtained stress-strain curves are shown in Figure 7 and Table 3 shows the Young Modulus, as determined by the tangent method from the linear regime at 3% of elongation in the elastic region.

Independently of the IL type and the fluorinated matrix, the incorporation of ILs induces a plasticizing effect in the typical thermoplastic behaviour of PVDF and copolymers. Figure 7a and 7b shows that the typical thermoplastic behaviour [45] of PVDF is maintained for composites, the main effect, as demonstrated for the [EMIM][TFSI]/PVDF composites (Figure 7a and Table 3), being a decrease in the Young Modulus and yield strength and an increase in yielding strain with increasing IL content increase. The lowest yield strength was observed upon the incorporation of 40 wt.% of [EMIM][TFSI]. This behaviour is also observed for PVDF-HFP composites. It is to notice that, [EMIM][TFSI]/PVDF and [EMIM][TFSI]/PVDF-HFP composites developed the higher strains, and in this sense, the lowest Young Modulus when compared with the corresponding [BMIM][SCN] composites.

### *3.4. Ionic conductivity value and electrochemical stability window*

Determining the ionic conductivity value of the SPE is essential to assess its applicability in the area of batteries [46, 47]. Typical Nyquist profiles for the 40 wt.% [BMIM][SCN] /PVDF composites at different temperatures are shown in Figure 8a, which shows that

the resistance decreases with increasing temperature in the composite. Further, the ionic conductivity value has calculated using equation 3.

Figure 8b and 8c shows the Arrhenius plots ( $\sigma = \sigma_0 e^{(-E_a/RT)}$ ,  $E_a$  is the apparent activation energy,  $R$  is the gas constant ( $8.314 \text{ J.mol}^{-1}.\text{K}^{-1}$ ) and  $\sigma_0$  is a pre-exponential factor) of the ionic conductivity value for the different IL/polymer composites in which the apparent activation energy ( $E_a$ ) was determined through the slope of the temperature dependence of the ionic conductivity. Figure 8b and 8c shows the ionic conductivities of IL/PVDF composites with different [EMIM][TFSI] contents as well as for 40 wt.% of [BMIM][SCN] in the temperature range from 25 to 100 °C. For the [EMIM][TFSI]/PVDF composites, it is observed that the ionic conductivity increases with increasing ionic liquid content due to the increase of the number of mobile ions and increased mobility due to the decrease in the degree of crystallinity [48]. In addition, the value of ionic conductivity increases with increasing temperature due to improvement of the segmental motion of polymer chains [49]. It is also observed that the ionic liquid type affects ionic conductivity value being related to the pristine value of the ionic conductivity value of ionic liquid (Figure 8b and 8c). Comparing both polymer matrices, the polymer matrix with the higher ionic conductivity value is PVDF-HFP due to the lower degree of crystallinity (Table 2). It is to notice that the diffusion process occurs in the amorphous phase of the polymer matrix and, therefore, a larger amorphous region content improves the ionic conductivity of the IL/polymer composites. The highest room temperature ionic conductivity value is  $0.15 \text{ mS.cm}^{-1}$  for 40 wt.% [BMIM][SCN]/PVDF-HFP, showing an apparent activation energy ( $E_a$ ) of  $6 \text{ kJ.mol}^{-1}$ .

In addition to the ionic conductivity value, the electrochemical stability window of the SPE is another important parameter to determine the battery device applicability [50]. Taking into account the high ionic conductivity value of polymer composites with 40 wt.% of [BMIM][SCN], the electrochemical stability window for these composites was determined by cyclic voltammetry (CV) over the 0.0 to 5.0 V potential range at a scan rate of  $0.1 \text{ mV.s}^{-1}$ . Figure 8d) shows that there are no oxidation/reduction peaks between 0.0 and 5.0 V, regardless of the polymer matrix, being very stable for their use in lithium-ion battery applications.

Therefore, considering the voltage range of the C-LiFePO<sub>4</sub> cathode, these composites show good electrochemical windows for application in solid-state lithium-ion batteries with this cathode.

### 3.5. Battery performance

Once the IL [BMIM][SCN] shows high ionic conductivity (Table 1) and leads to composites with high ionic conductivity (Figure 8b and 8c), the battery performance was evaluated in SPE prepared with [BMIM][SCN] composites with PVDF and PVDF-HFP. To assess the applicability of IL/polymer composites SPE in solid-state batteries, Li/SPE/C-LiFePO<sub>4</sub> half-cells were produced with [BMIM][SCN]/PVDF and [BMIM][SCN]/PVDF-HFP with 40 wt.% IL content. Battery performance was determined at room temperature and at the C/8 rate in which the battery is charged and discharged in eight hours.

Figure 9a shows the fifth charge–discharge capacity curves of the all-solid-state Li/SPE/C-LiFePO<sub>4</sub> cells with [BMIM][SCN]/PVDF or [BMIM][SCN]/PVDF-HFP at C/8 rate.

Regardless of the polymeric matrix, Figure 9a shows the typical charge/discharge voltage profiles reflecting lithium disinsertion in the charging process and lithium insertion in the discharge process corresponding to the Fe<sup>2+</sup>/Fe<sup>3+</sup> process [34]. As shown in Figure 9a, the cell with PVDF polymer exhibits the highest discharge capacity with about 148 mAh.g<sup>-1</sup>, being the one for the PVDF-HFP composites 124 mAh.g<sup>-1</sup>, which correspond to 87% and 72%, respectively, of the discharge capacity theoretical value (170 mAh.g<sup>-1</sup>). The differences are related to the low Young modulus of the PVDF polymer [34].

Figure 9b shows the discharge capacity values for both SPEs over 50 charge-discharge cycles at room temperature and a C/8 rate, allowing to evaluate the cycling stability.

It is observed that the discharge capacity value of PVDF-HFP with [BMIM][SCN] is very stable over 50 cycles due to improvement of the interfacial contact with the electrodes originated by low degree of crystallinity. The low degree of crystallinity allows that a stable interface between the electrolyte and electrode forms after a few cycles, resulting in the stable electrical performance during the cycling life [51]. For this SPE, the capacity fade over 50 cycles is 16 % against the one observed for PVDF, which is 70 %. In addition, the Coulomb efficiency (figure 9b) remains above 98 % during the cycle life test, demonstrating a significant improvement in cycle stability. As demonstrated, the polymer matrix has an important role in the stabilization of the interface between the electrodes and the SPEs.

To better understand the electrochemical performance of Li/SPE/C-LiFePO<sub>4</sub> half-cells, the EIS spectra of these cells were recorded before and after the cycle, as shown in the Nyquist plots of Figure 9c and 9d, respectively.

The Nyquist plots presented in figure 9c and d) before and after cycling are characterized by a semicircle (overall resistance, which is the sum of the Ohmic resistance, that represents the contact film resistance and resistance contributions from the charge-transfer reaction resistance) in the high and medium frequency regions and a straight line characterized by Warburg element, associated with the Li<sup>+</sup> diffusion process in the low frequency regions. For the PVDF-HFP polymer matrix, the overall resistance before and after cycling are 515 Ω and 1450 Ω, respectively, the increase being attributed to the formation of a SEI layer during cycling [52]. The same behavior is observed for the PVDF polymeric matrix.

Considering the excellent charge-discharge results presented in Figure 9a and 9b at room temperature, Table 4 shows the ionic conductivity and discharge capacity values for different SPEs based on ILs, lithium salts and polymers reported in the literature for the same electrode.

Table 4 shows that the electrochemical results of the different SPEs are evaluated at high temperatures above 50 °C, contrary to what has been evaluated in this work, in which, at room temperature and C/8-rate, these SPEs present excellent discharge behavior, mainly for the PVDF-HFP polymer, with low capacity fade.

Thus, the present work demonstrates that it is possible to prepare SPEs, working at room temperature and with high ionic conductivity, based on ionic liquid and PVDF-HFP for the next generation of solid-state lithium batteries.

#### **4. Conclusion**

IL/ PVDF and IL/PVDF-HFP composites, comprising different ILs ([EMIM][TFSI] and [BMIM][SCN]) were developed for SPEs in batteries applications.

Independently of the IL type and fluorinated matrix, the incorporation of the ILs into the polymer matrix induces an increase in the surface wettability of the samples.

Both ILs promote the crystallization of the PVDF and PVDF-HFP into the polar  $\beta$  phase of the polymer and a reduction of the degree of crystallinity, as a result of the ion-dipole electrostatic interactions between the IL and fluorinated matrix. Further, increasing IL content leads to a plasticizing behaviour of the samples.

The highest room temperature ionic conductivity value of  $0.15 \text{ mS.cm}^{-1}$  is observed for [BMIM][SCN]/PVDF-HFP with 40 wt.% IL content. Additionally, this composite presents an excellent electrochemical stability between 0.0 V and 5.0 V, suitable for lithium-ion batteries with electrodes based on C-LiFePO<sub>4</sub>.

The electrochemical performance of the Li/C-LiFePO<sub>4</sub> cells with different SPEs is excellent at C/8, showing  $148 \text{ mAh.g}^{-1}$  and  $124 \text{ mAh.g}^{-1}$  for [BMIM][SCN]/PVDF and [BMIM][SCN]/PVDF-HFP SPEs, respectively. After 50 cycles at C/8-rate, the capacity fade of the batteries with [BMIM][SCN]/PVDF-HFP is 16 %, which is lower when compared with [BMIM][SCN]/PVDF (70 %).

It is concluded that is possible to produce solid-state lithium-ion batteries based on SPEs prepared through IL/fluorinated polymer composites, with excellent electrical and electrochemical results at room temperature.

### Acknowledgements

Work supported by the Portuguese Foundation for Science and Technology (FCT) under strategic funding UID/FIS/04650/2020 and UID/QUI/0686/2020, project PTDC/FIS-MAC/28157/2017, and Grants SFRH/BD/140842/2018 (J.C.B.), SFRH/BPD/121526/2016 (D.M.C), CEECIND/00833/2017 (R.G.) and SFRH/BPD/112547/2015 (C.M.C.). Financial support from the Basque Government Industry Department under the ELKARTEK and HAZITEK programs is also acknowledged.

### References

1. Costa, C.M., R. Gonçalves, and S. Lanceros-Méndez, *Recent advances and future challenges in printed batteries*. Energy Storage Materials, 2020. **28**: p. 216-234.

2. Costa, C.M., et al., *Recent advances on separator membranes for lithium-ion battery applications: From porous membranes to solid electrolytes*. Energy Storage Materials, 2019. **22**: p. 346-375.
3. Chernova, N.A., et al., *What can we learn about battery materials from their magnetic properties?* Journal of Materials Chemistry, 2011. **21**(27): p. 9865-9875.
4. Whittingham, M.S., *Electrical energy storage and intercalation chemistry*. Science, 1976. **192**(4244): p. 1126-1127.
5. Nishi, Y., *The development of lithium ion secondary batteries*. The Chemical Record, 2001. **1**(5): p. 406-413.
6. Abraham, K., *Prospects and limits of energy storage in batteries*. The journal of physical chemistry letters, 2015. **6**(5): p. 830-844.
7. Miranda, D., et al., *Theoretical simulation of the optimal relation between active material, binder and conductive additive for lithium-ion battery cathodes*. Energy, 2019. **172**: p. 68-78.
8. Costa, C.M., M.M. Silva, and S. Lanceros-Mendez, *Battery separators based on vinylidene fluoride (VDF) polymers and copolymers for lithium ion battery applications*. Rsc Advances, 2013. **3**(29): p. 11404-11417.
9. Lisbona, D. and T. Snee, *A review of hazards associated with primary lithium and lithium-ion batteries*. Process Safety and Environmental Protection, 2011. **89**(6): p. 434-442.
10. Costa, C.M., et al., *Recent advances on separator membranes for lithium-ion battery applications: From porous membranes to solid electrolytes*. Energy Storage Materials, 2019.
11. Barbosa, J., et al., *Recent advances in poly (vinylidene fluoride) and its copolymers for lithium-ion battery separators*. Membranes, 2018. **8**(3): p. 45.
12. Li, J., et al., *Solid electrolyte: the key for high-voltage lithium batteries*. Advanced Energy Materials, 2015. **5**(4): p. 1401408.
13. Kato, Y., et al., *High-power all-solid-state batteries using sulfide superionic conductors*. Nature Energy, 2016. **1**(4): p. 16030.
14. Zhang, Y., et al., *The effects of the size and content of BaTiO<sub>3</sub> nanoparticles on solid polymer electrolytes for all-solid-state lithium-ion batteries*. Journal of Solid State Electrochemistry, 2019. **23**(3): p. 749-758.



15. Li, D., et al., *Enhancement of electrochemical performance of lithium-ion battery by single-ion conducting polymer addition in ceramic-coated separator*. Journal of Materials Science, 2018. **53**(15): p. 11038-11049.
16. Choudhury, S., et al., *Soft Colloidal Glasses as Solid-State Electrolytes*. Chemistry of Materials, 2018. **30**(17): p. 5996-6004.
17. Li, X., et al., *Preparation and performance of poly(ethylene oxide)-based composite solid electrolyte for all solid-state lithium batteries*. Journal of Applied Polymer Science, 2019. **136**(19): p. 47498.
18. Ahmad, A.L., U.R. Farooqui, and N.A. Hamid, *Synthesis and characterization of porous poly(vinylidene fluoride-co-hexafluoro propylene) (PVDF-co-HFP)/poly(aniline) (PANI)/graphene oxide (GO) ternary hybrid polymer electrolyte membrane*. Electrochimica Acta, 2018. **283**: p. 842-849.
19. Nunes-Pereira, J., et al., *Li-ion battery separator membranes based on poly(vinylidene fluoride-trifluoroethylene)/carbon nanotube composites*. Solid State Ionics, 2013. **249-250**: p. 63-71.
20. Whba, R.A.G., et al., *Influence of binary lithium salts on 49% poly(methyl methacrylate) grafted natural rubber based solid polymer electrolytes*. Arabian Journal of Chemistry, 2020. **13**(1): p. 3351-3361.
21. Arya, A. and A.L. Sharma, *Structural, microstructural and electrochemical properties of dispersed-type polymer nanocomposite films*. Journal of Physics D: Applied Physics, 2018. **51**(4): p. 045504.
22. Zeng, H., et al., *Enhanced cycling performance for all-solid-state lithium ion battery with LiFePO<sub>4</sub> composite cathode encapsulated by poly (ethylene glycol) (PEG) based polymer electrolyte*. Solid State Ionics, 2018. **320**: p. 92-99.
23. Wei, Z., et al., *Superior lithium ion conduction of polymer electrolyte with comb-like structure via solvent-free copolymerization for bipolar all-solid-state lithium battery*. Journal of Materials Chemistry A, 2018. **6**(27): p. 13438-13447.
24. Yang, G., et al., *Ion Pair Integrated Organic-Inorganic Hybrid Electrolyte Network for Solid-State Lithium Ion Batteries*. Energy Technology, 2018. **6**(12): p. 2319-2325.
25. Wang, A., et al., *Polyimide-Based Self-Standing Polymer Electrolyte Membrane for Lithium-Ion Batteries*. Energy Technology, 2018. **6**(2): p. 326-332.
26. Song, J.Y., Y.Y. Wang, and C.C. Wan, *Review of gel-type polymer electrolytes for lithium-ion batteries*. Journal of Power Sources, 1999. **77**(2): p. 183-197.

27. Lei, Z., et al., *Introduction: ionic liquids*. 2017, ACS Publications.
28. Holbrey, J. and K. Seddon, *Ionic liquids*. Clean products and processes, 1999. **1**(4): p. 223-236.
29. Olivier-Bourbigou, H., L. Magna, and D. Morvan, *Ionic liquids and catalysis: Recent progress from knowledge to applications*. Applied Catalysis A: General, 2010. **373**(1-2): p. 1-56.
30. Correia, D., et al., *Ionic and conformational mobility in poly (vinylidene fluoride)/ionic liquid blends: Dielectric and electrical conductivity behavior*. Polymer, 2018. **143**: p. 164-172.
31. Xu, P., et al., *Enhanced dc conductivity and conductivity relaxation in PVDF/ionic liquid composites*. Materials Letters, 2017. **206**: p. 60-63.
32. Ribeiro, C., et al., *Electroactive poly (vinylidene fluoride)-based structures for advanced applications*. Nature protocols, 2018. **13**(4): p. 681.
33. Martins, P., A. Lopes, and S. Lanceros-Mendez, *Electroactive phases of poly (vinylidene fluoride): Determination, processing and applications*. Progress in polymer science, 2014. **39**(4): p. 683-706.
34. Gören, A., et al., *High performance screen-printed electrodes prepared by a green solvent approach for lithium-ion batteries*. Journal of Power Sources, 2016. **334**: p. 65-77.
35. Martins, P., et al., *Correlation between crystallization kinetics and electroactive polymer phase nucleation in ferrite/poly (vinylidene fluoride) magnetoelectric nanocomposites*. The Journal of Physical Chemistry B, 2012. **116**(2): p. 794-801.
36. Mejri, R., et al., *Effect of ionic liquid anion and cation on the physico-chemical properties of poly (vinylidene fluoride)/ionic liquid blends*. European Polymer Journal, 2015. **71**: p. 304-313.
37. Meira, R.M., et al., *Ionic-Liquid-Based Electroactive Polymer Composites for Muscle Tissue Engineering*. ACS Applied Polymer Materials, 2019.
38. Xing, C., et al., *Effect of a Room-Temperature Ionic Liquid on the Structure and Properties of Electrospun Poly(vinylidene fluoride) Nanofibers*. ACS Applied Materials & Interfaces, 2014. **6**(6): p. 4447-4457.
39. Biswas, A., et al., *Comparison of the thermal stability of the  $\alpha$ ,  $\beta$  and  $\gamma$  phases in poly(vinylidene fluoride) based on in situ thermal Fourier transform infrared spectroscopy*. Phase Transitions, 2017. **90**(12): p. 1205-1213.

40. Bormashenko, Y., et al., *Vibrational spectrum of PVDF and its interpretation*. Polymer Testing, 2004. **23**(7): p. 791-796.
41. Sousa, R.E., et al., *Microstructural variations of poly(vinylidene fluoride co-hexafluoropropylene) and their influence on the thermal, dielectric and piezoelectric properties*. Polymer Testing, 2014. **40**: p. 245-255.
42. Kiefer, J., J. Fries, and A. Leipertz, *Experimental Vibrational Study of Imidazolium-Based Ionic Liquids: Raman and Infrared Spectra of 1-Ethyl-3-methylimidazolium Bis(Trifluoromethylsulfonyl)imide and 1-Ethyl-3-methylimidazolium Ethylsulfate*. Applied Spectroscopy, 2007. **61**(12): p. 1306-1311.
43. Cai, X., et al., *A critical analysis of the  $\alpha$ ,  $\beta$  and  $\gamma$  phases in poly(vinylidene fluoride) using FTIR*. RSC Advances, 2017. **7**(25): p. 15382-15389.
44. Correia, D., et al., *Ionic Liquid Cation Size-Dependent Electromechanical Response of Ionic Liquid/Poly (vinylidene fluoride)-Based Soft Actuators*. The Journal of Physical Chemistry C, 2019. **123**(20): p. 12744-12752.
45. Costa, C.M., et al., *Microscopic origin of the high-strain mechanical response of poled and non-poled poly(vinylidene fluoride) in the  $\beta$ -phase*. Journal of Non-Crystalline Solids, 2008. **354**(32): p. 3871-3876.
46. Jr., D.T.H. and N.P. Balsara, *Polymer Electrolytes*. Annual Review of Materials Research, 2013. **43**(1): p. 503-525.
47. Yao, P., et al., *Review on Polymer-Based Composite Electrolytes for Lithium Batteries*. Frontiers in Chemistry, 2019. **7**(522).
48. Leones, R., et al., *Development of solid polymer electrolytes based on poly(vinylidene fluoride-trifluoroethylene) and the [N1 1 1 2(OH)][NTf2] ionic liquid for energy storage applications*. Solid State Ionics, 2013. **253**: p. 143-150.
49. Leones, R., et al., *Effect of Ionic Liquid Anion Type in the Performance of Solid Polymer Electrolytes Based on Poly(Vinylidene fluoride-trifluoroethylene)*. Electroanalysis, 2015. **27**(2): p. 457-464.
50. Kim, H.-S., P. Periasamy, and S.-I. Moon, *Electrochemical properties of the Li-ion polymer batteries with P(VdF-co-HFP)-based gel polymer electrolyte*. Journal of Power Sources, 2005. **141**(2): p. 293-297.
51. Li, C., et al., *A novel composite solid polymer electrolyte based on copolymer P(LA-co-TMC) for all-solid-state lithium ionic batteries*. Solid State Ionics, 2018. **321**: p. 8-14.

52. Guo, J., et al., *Cyclability study of silicon–carbon composite anodes for lithium-ion batteries using electrochemical impedance spectroscopy*. *Electrochimica Acta*, 2011. **56**(11): p. 3981-3987.
53. Tao, C., et al., *A promising TPU/PEO blend polymer electrolyte for all-solid-state lithium ion batteries*. *Electrochimica Acta*, 2017. **257**: p. 31-39.
54. Li, X., et al., *Composite electrolytes of pyrrolidone-derivatives-PEO enable to enhance performance of all solid state lithium-ion batteries*. *Electrochimica Acta*, 2019. **293**: p. 25-29.
55. Baik, J.-H., et al., *Solid polymer electrolytes containing poly(ethylene glycol) and renewable cardanol moieties for all-solid-state rechargeable lithium batteries*. *Polymer*, 2016. **99**: p. 704-712.
56. Bao, J., et al., *Solid electrolyte based on waterborne polyurethane and poly(ethylene oxide) blend polymer for all-solid-state lithium ion batteries*. *Solid State Ionics*, 2018. **320**: p. 55-63.
57. Polu, A.R. and H.-W. Rhee, *Ionic liquid doped PEO-based solid polymer electrolytes for lithium-ion polymer batteries*. *International Journal of Hydrogen Energy*, 2017. **42**(10): p. 7212-7219.

## Figure captions

**Figure 1** - Schematic representation of the procedure used to IL/PVDF and PVDF-HFP films preparation.

**Figure 2** - Schematic representation of the battery prototype fabrication.

**Figure 3** - Cross section images of (a-c) IL/PVDF composites and (d-e) IL/PVDF-HFP composites, with different ILs type and content.

**Figure 4** - Water contact angle for a) pristine PVDF and [EMIM][TFSI]/PVDF composite films varying IL content and b) pristine PVDF composites with both IL types for a maximum IL content of 40% wt.

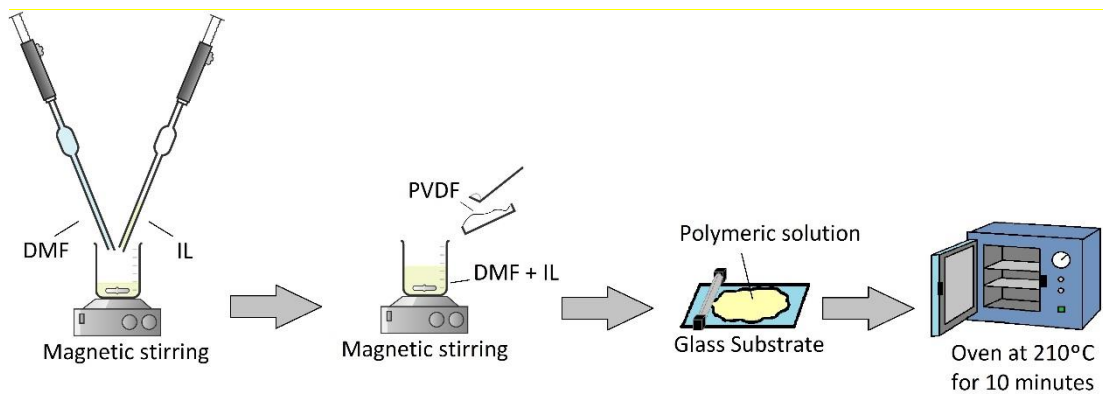
**Figure 5** - FTIR-ATR spectra of a) pristine PVDF with different IL type and content, b) PVDF-HFP with 40% wt. [EMIM][TFSI] and [BMIM][SCN].

**Figure 6** - DSC scans for a) PVDF and b) PVDF-HFP pristine and IL composites

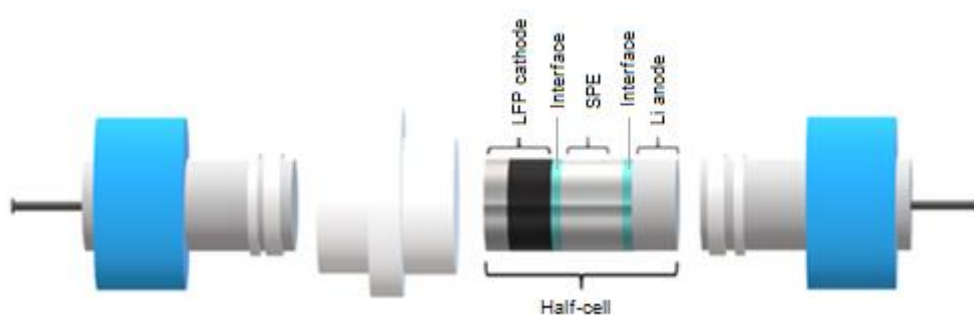
**Figure 7** - Stress–strain curves of the a) IL/PVDF and b) PVDF-HFP composite films

**Figure 8** – a) Nyquist plot of the [BMIM][SCN](40%)/PVDF composites at different temperatures. The Arrhenius plots for the ionic conductivities of the IL/polymer composites based on b) PVDF and c) PVDF-HFP. d) Cyclic voltammogram of the composite with 40 % wt of [BMIM][SCN] within PVDF and PVDF-HFP matrix measured at room temperature and at scan rate of 100 mV.s<sup>-1</sup>.

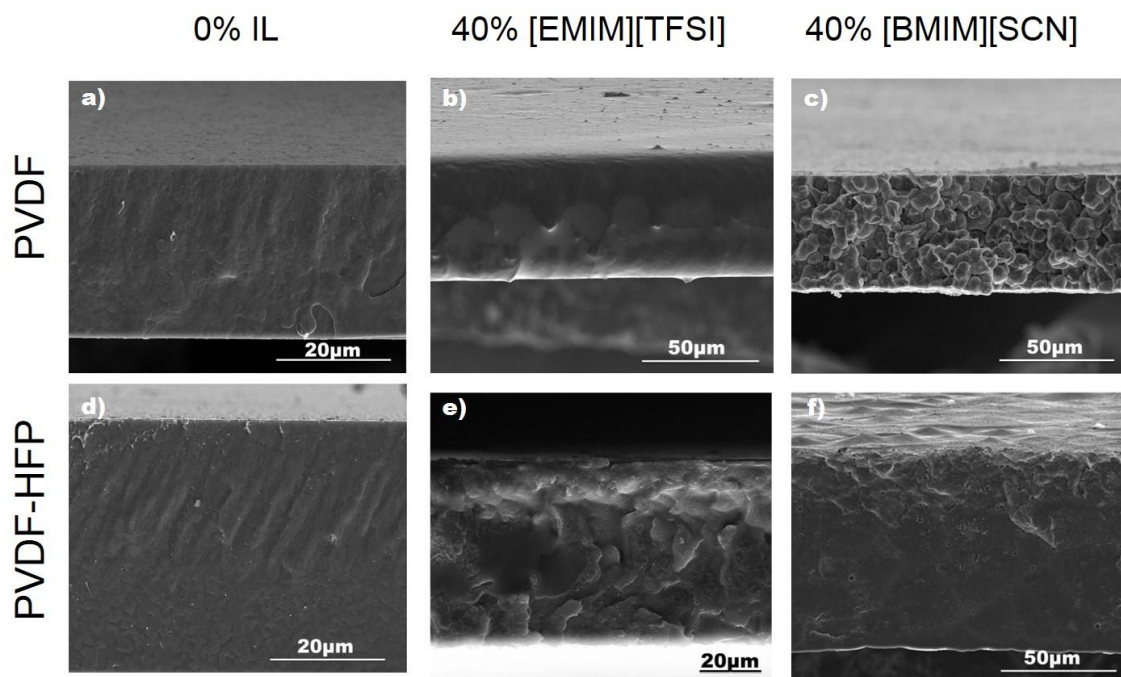
**Figure 9** – All-solid-state Li/SPE/C-LiFePO<sub>4</sub> cells with [BMIM][SCN]/PVDF and [BMIM][SCN]/PVDF-HFP: a) 5<sup>th</sup> charge and discharge cycle room temperature profiles at a rate of C/8, b) rate performance as a function of the cycle number and impedance spectroscopy of the cathodic half-cells c) before and d) after cycling.



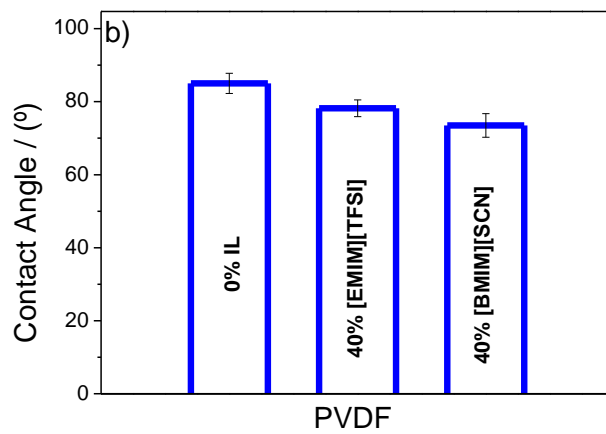
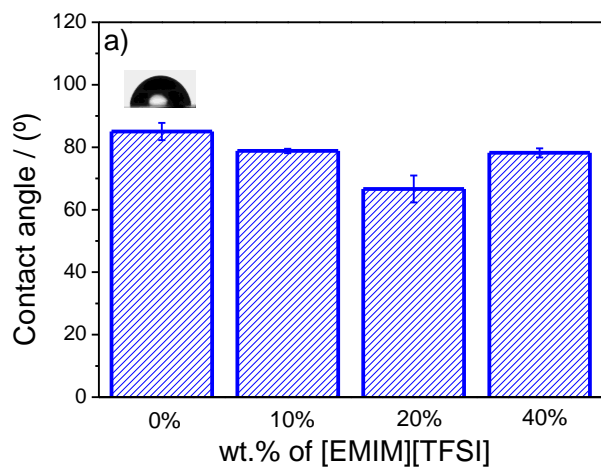
**Figure 1**



**Figure 2**



**Figure 3**



**Figure 4**

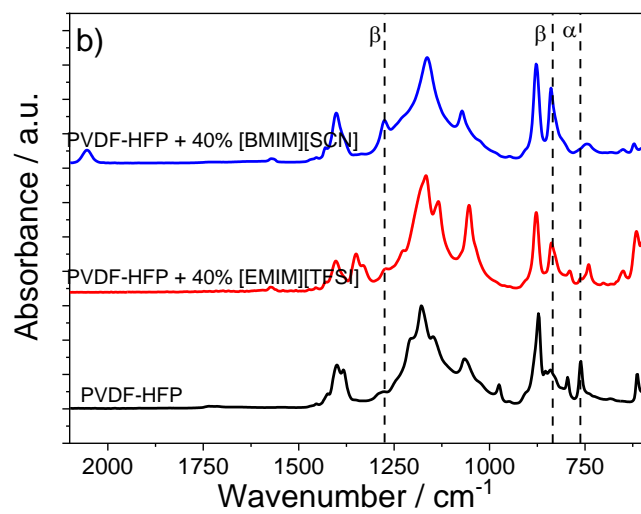
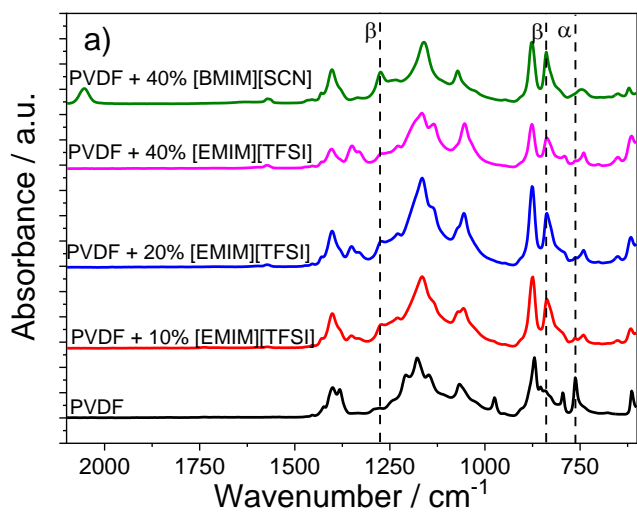


Figure 5

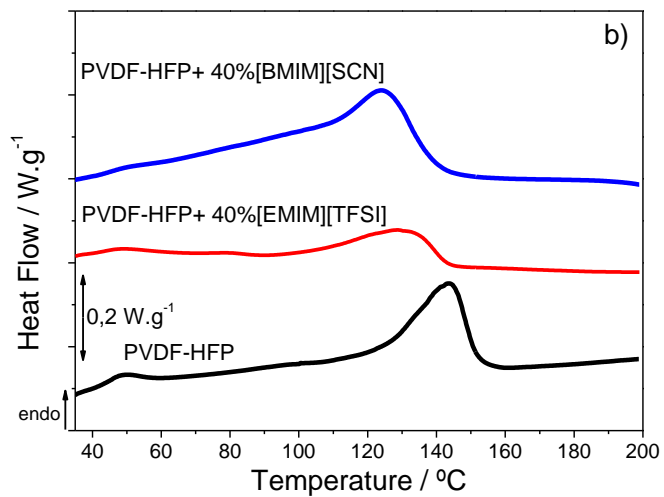
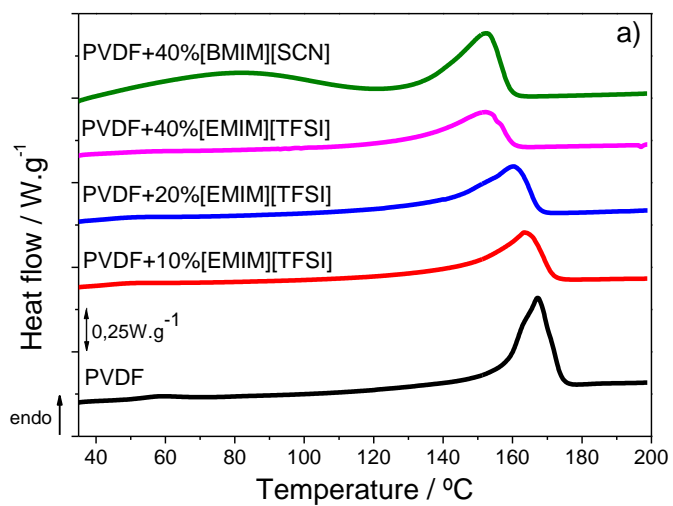
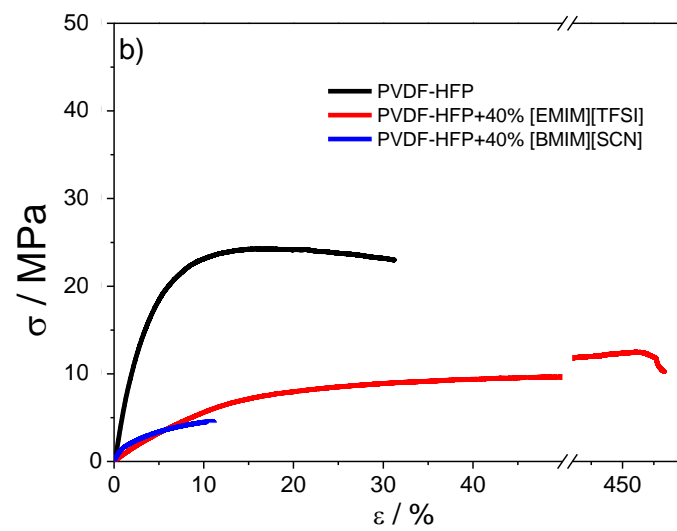
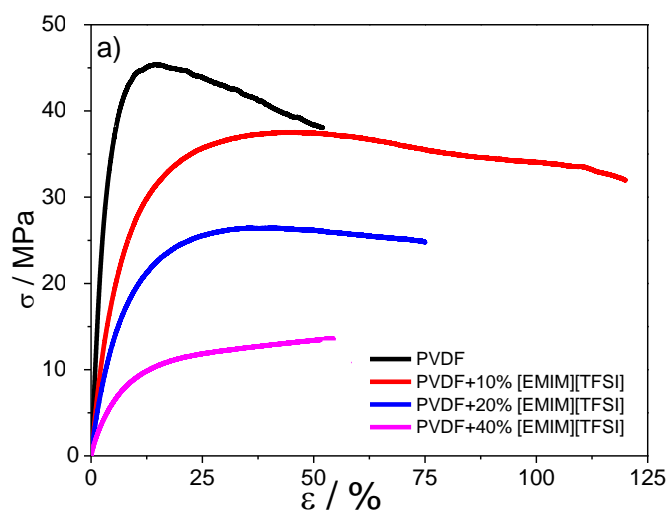


Figure 6





**Figure 7**

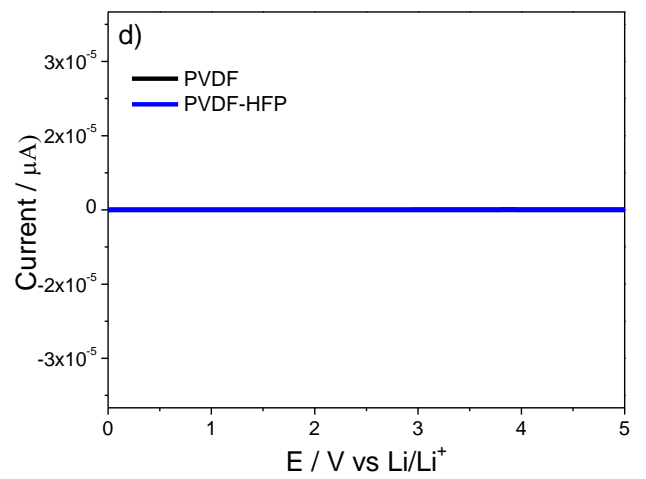
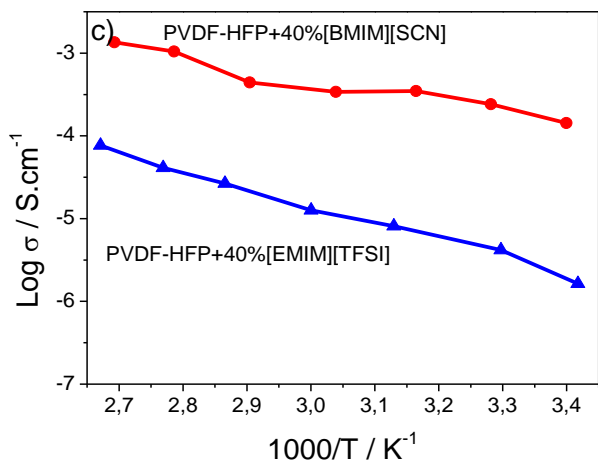
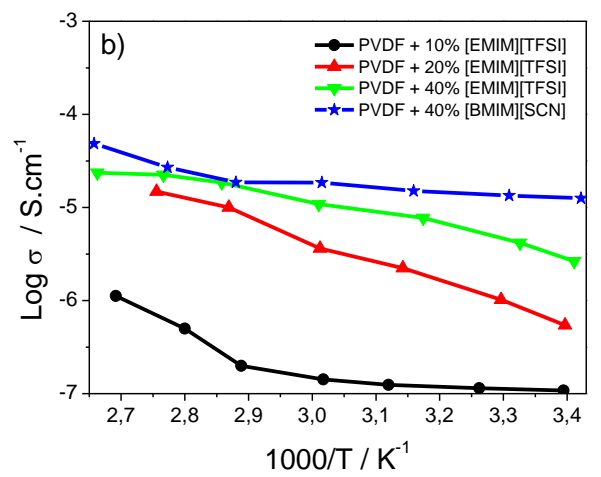
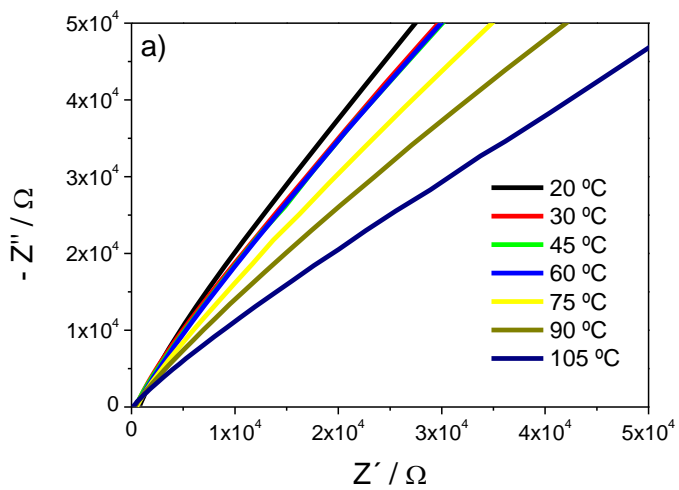
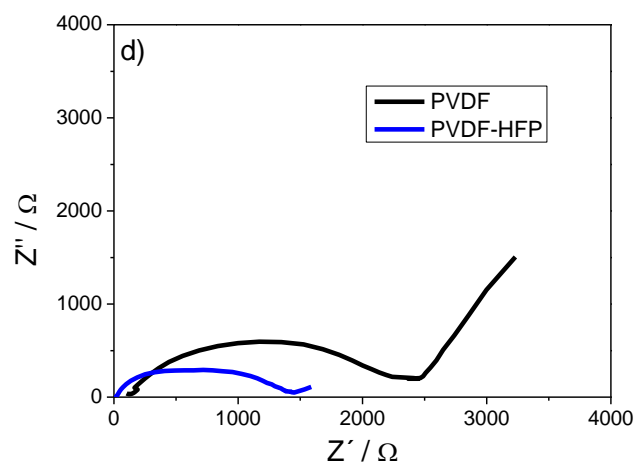
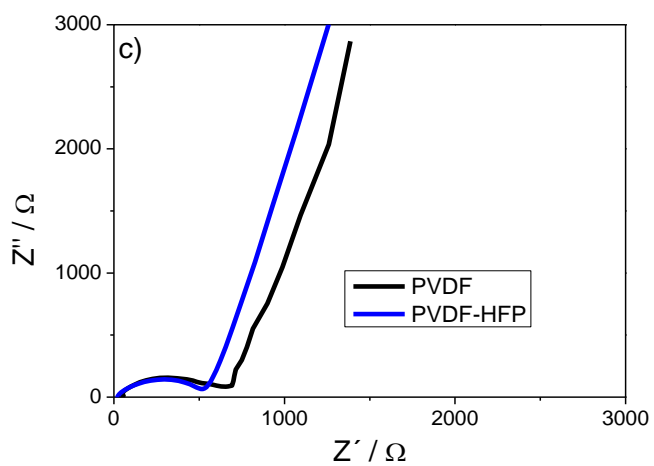
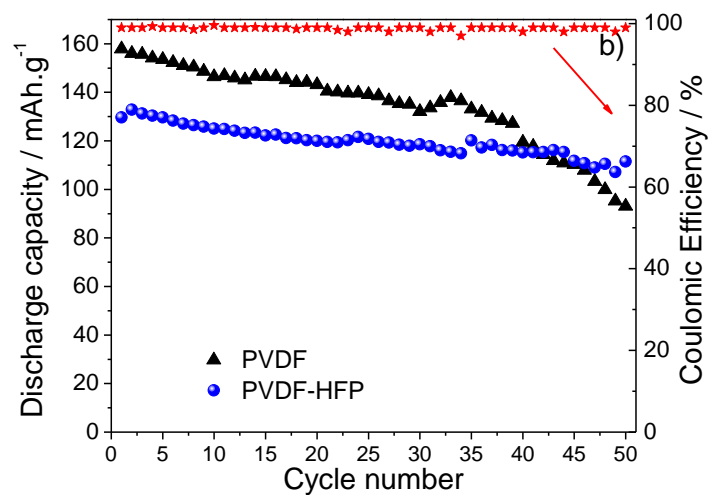
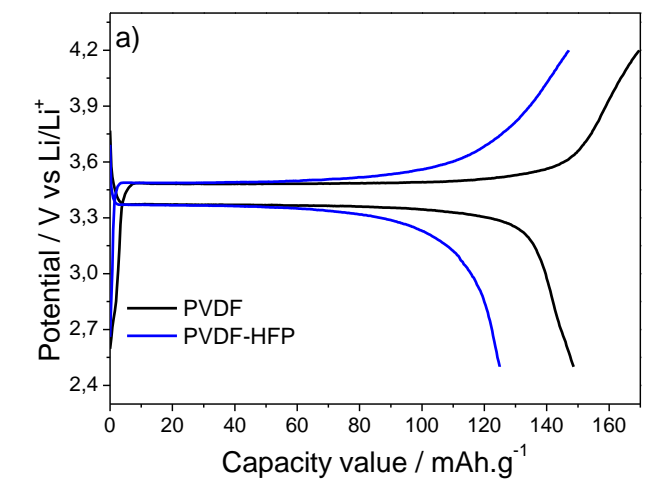



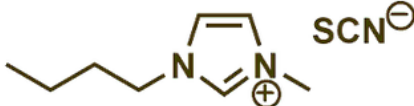
Figure 8



**Figure 9**

## Table captions

**Table 1** - Main properties of the different ILs used in this work.

Ionic liquid	Structure	M / g.mol <sup>-1</sup>	$\rho$ / kg.m <sup>-3</sup>	$\sigma$ / mS.cm <sup>-1</sup> at 25 °C	$\eta$ / cP
[EMIM][TFSI]		391.31	1.52	6.63	39.4
[BMIM][SCN]		197.30	1.07	8.98	35.9

**Table 2** -  $\beta$  phase content, melting temperature and degree of crystallinity  $\chi_c$ , of the different composites films.

Polymer	% IL wt.	$\beta$ phase $\pm 3$ (%)	Tm $\pm 1$ (°C)	Xc $\pm 2$ (%)
PVDF	0%	34	163	35
	[EMIM][TFSI](10%)	84	167	38
	[EMIM][TFSI](20%)	87	160	31
	[EMIM][TFSI](40%)	83	152	28
	[BMIM][SCN](40%)	100	152	36
PVDF-HFP	0%	39	143	23
	[EMIM][TFSI](40%)	82	129	12
	[BMIM][SCN](40%)	100	120	16

**Table 3** - Young modulus and yield strength for the different samples.

Polymer	IL content (wt.%)	Young modulus (MPa)
	0%	713.0±204
PVDF	[EMIM][TFSI](10%)	461.0±182
	[EMIM][TFSI](20%)	290.0±23.0
	[EMIM][TFSI](40%)	141.0±9.5
	[BMIM][SCN](40%)	151.0±67.4
	0%	510±121
PVDF-HFP	[EMIM][TFSI](40%)	56.2±5.0
	[BMIM][SCN](40%)	162.5±22.9

**Table 4** - SPEs based on ILs, lithium salts and polymers.

Polymer	Fillers	Conductivity (S/cm)	Discharge capacity (mAh/g)	Ref
TPU/PEO	LiTFSI	$5.3 \times 10^{-4}$ (60°C)	140 (C/5)	[53]
PEO	LiTFSI	$2.5 \times 10^{-4}$ (80°C)	140 (C/5)	[54]
PEGMA:HCPM	LiTFSI	$1.9 \times 10^{-4}$ (60°C)	200 (V <sub>2</sub> O <sub>5</sub> at C/10)	[55]
P(LA-co-TMC)	LiTFSI	$6.5 \times 10^{-4}$ (55°C)	123 (C/10)	[51]
PEO:WPU	LiTFSI	$3.1 \times 10^{-3}$ (80°C)	160 (C/5)	[56]
PEO	LiDFOB- EMImTFSI	$9.4 \times 10^{-6}$ (25°C)	155 (C/10)	[57]
PVDF	[BMIM][SCN]	$0.013 \times 10^{-3}$ (25°C)	148 (C/8)	This work
PVDF-HFP	[BMIM][SCN]	$0.15 \times 10^{-3}$ (25°C)	124 (C/8)	This work